ployed in order to increase maximum tube current. The high-voltage main condenser is charged to 55 kV by the power supply, and electric charges in the condenser are discharged to the tube after triggering the cathode electrode with the trigger device. The plasma flash x-rays are then produced.

2.2 X-ray tube

The x-ray tube is a demountable cold cathode triode that is connected to the turbo-molecular pump with a pressure of approximately 1 mPa (Fig. 2). This tube consists of the following major parts: a pipe-shaped carbon cathode with a bore diameter of 10.0 mm, a trigger electrode made from copper wire, a stainless steel vacuum chamber, a nylon insulator, a polyethylene terephthalate polyester film (Mylar) x-ray window 0.25 mm in thickness, and a rod-shaped molybdenum target 2.0 mm in diameter with a tip angle of 60°. The distance between the anode and cathode electrodes is approximately 20 mm, and the trigger electrode is set in the cathode electrode. As electron beams from the cathode electrode are roughly converged to the target by the electric field in the tube, evaporation leads to the formation of a weakly ionized linear plasma, consisting of molybdenum ions and electrons, around the fine target.

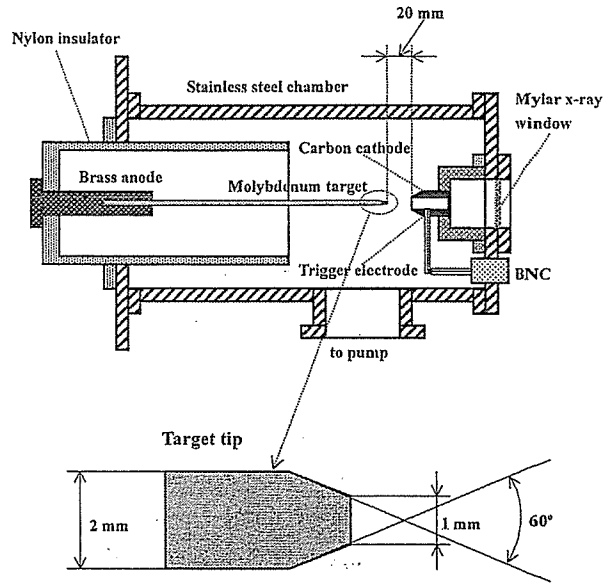

Fig. 2. Schematic drawing of the flash x-ray tube with a rod target.

2.3 Principle of characteristic x-ray irradiation

In the linear plasma, bremsstrahlung photons with energies higher than the K-absorption edge are effectively absorbed and are converted into fluorescent x-rays (Fig. 3). The plasma then transmits the fluorescent rays easily, and bremsstrahlung rays with energies lower than the K-edge are also absorbed by the plasma. In addition, because bremsstrahlung rays are not emitted in the direction opposite that of electron acceleration, intense characteristic x-rays are generated from the plasma-axial direction.

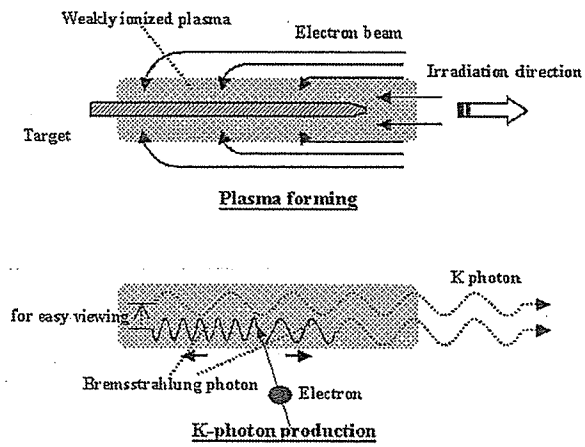

Fig. 3. K-photon irradiation from the plasma.

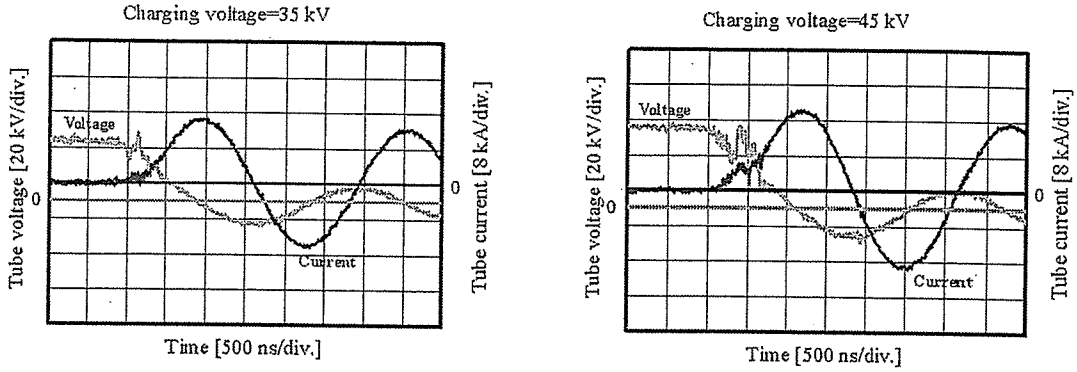

Fig. 4. Tube voltages and currents with a charging voltage of (a) 35 kV, (b) 45 kV, and (c) 55 kV.

3. Characteristics

3.1 Tube voltage and current

Tube voltage and current were measured by a high-voltage divider with an input impedance of 1 GΩ and a current transformer, respectively. Figure 4 shows the time relation for the tube voltage and current. At the indicated charging voltages, they roughly displayed damped oscillations. When the charging voltage was increased, both the maximum tube voltage and current increased. At a charging voltage of 55 kV, the maximum tube voltage was almost equal to the charging voltage of the main condenser, and the maximum tube current was approximately 20 kA.

3.2 X-ray output

X-ray output pulse was detected using a combination of a plastic scintillator and a photomultiplier (Fig. 5). The x-ray pulse height substantially increased with corresponding increases in the charging voltage, but there was a big decrease when a monochromatic molybdenum filter of 30μm in thickness was inserted. The x-ray pulse widths were about 700 ns, and the time-integrated x-ray intensity measured by a thermoluminescence dosimeter (Kyokko TLD Reader 1500 having MSO-R elements without energy compensation) had a value of about 35μC/kg at 1.0 m from the x-ray source with a charging voltage of 50 kV.

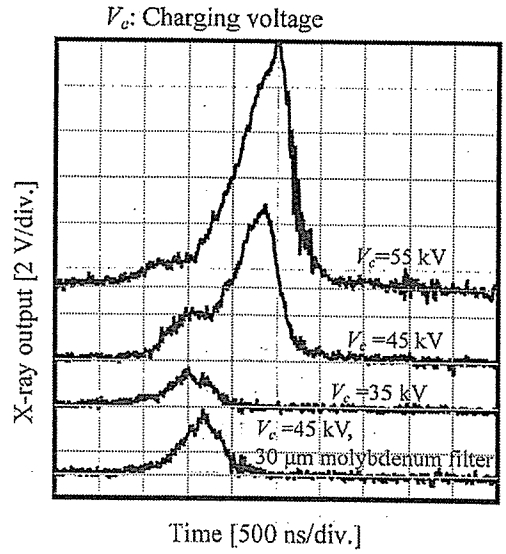

Fig. 5. X-ray outputs at the indicated conditions.

3.3 X-ray source

In order to measure images of the plasma x-ray source, we employed a pinhole camera with a hole diameter of 100μm (Fig. 6). When the charging voltage was increased, the plasma x-ray source grew, and both spot dimension and intensity increased. In contrast, both the dimension and intensity decreased upon insertion of the monochromatic filter.

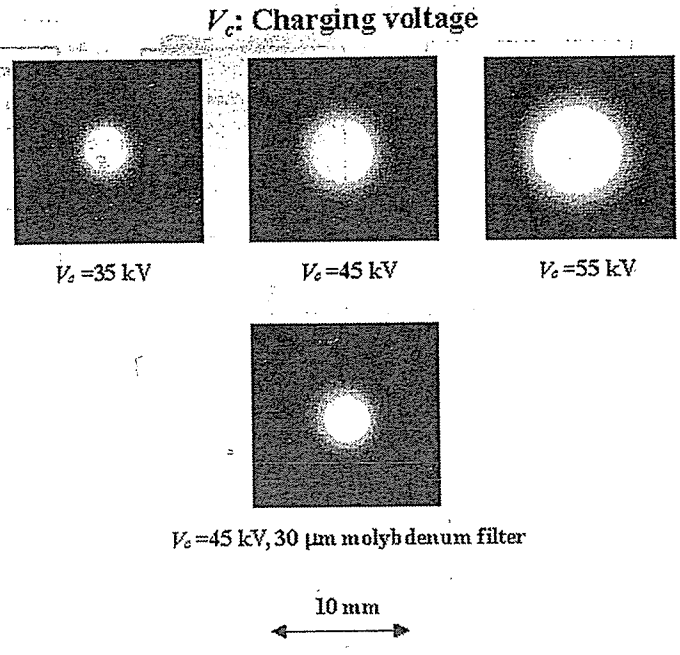

Fig. 6. Images of the plasma x-ray source.

3.4 X-ray spectra

X-ray spectra from the plasma source were measured by a transmission-type spectrometer[19] (Fig. 7) with a lithium fluoride curved crystal 0.5 mm in thickness. The spectra were taken by a computed radiography (CR) system (Konica Regius 150)[20] with a wide dynamic range, and relative x-ray intensity was calculated from Dicom digital data. Figure 8 shows measured spectra from the molybdenum target. In fact, we observed quite sharp lines of K-series characteristic x-rays such as lasers, while bremsstrahlung rays were hardly detected. The characteristic x-ray intensity substantially increased with corresponding increases in the charging voltage and decreased with insertion of the filter.

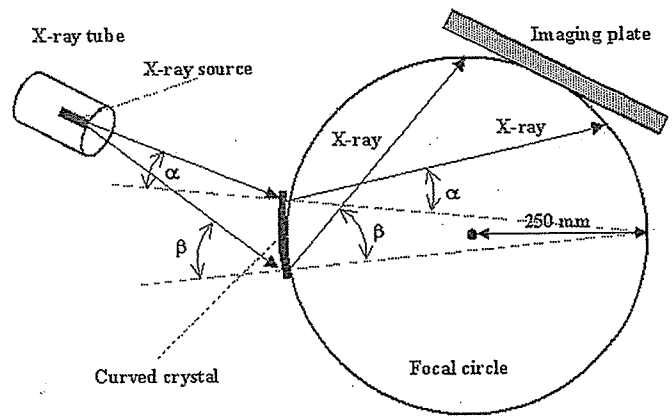

Fig. 7. Transmission-type spectrometer using an imaging plate.

3.5 X-ray divergence by slits

In order to ascertain the difference in characteristics between x-rays from a conventional tube and these from the plasma tube, we employed two lead slits in order to measure the divergence of the x-rays (Fig. 9). As compared with incoherent x-rays from a conventional tube with a tungsten target, the characteristic x-rays from the linear plasma were diffused greatly after passing through the two slits (Fig. 10).

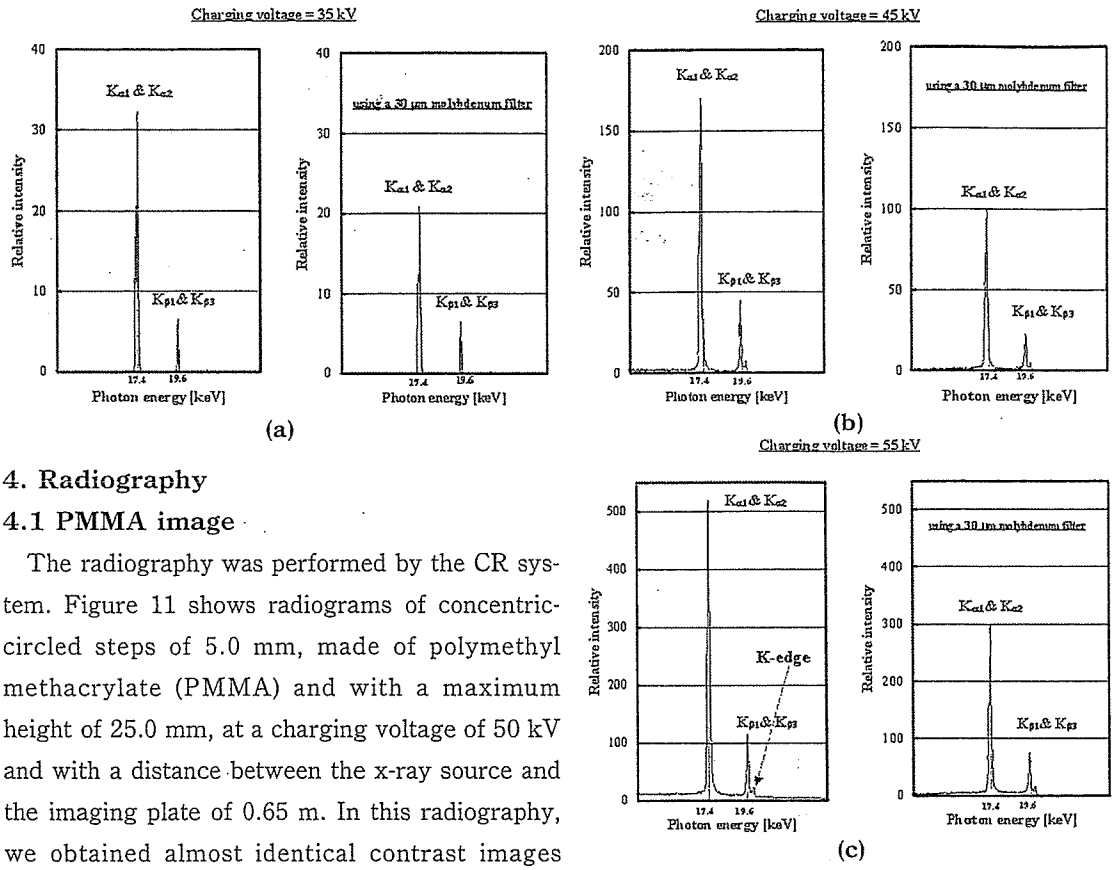

Fig. 8 X-ray spectra from weakly ionized molybdenum plasma with a charging voltage of (a) 35 kV, (b) 45 kV, and (c) 55 kV.

4. Radiography

4.1 PMMA image

The radiography was performed by the CR system. Figure 11 shows radiograms of concentric-circled steps of 5.0 mm, made of polymethyl methacrylate (PMMA) and with a maximum height of 25.0 mm, at a charging voltage of 50 kV and with a distance between the x-ray source and the imaging plate of 0.65 m. In this radiography, we obtained almost identical contrast images regardless of whether the 30μm-thick molybdenum filter was employed or not. The image qualities of radiograms taken by the plasma generator were somewhat soft compared with a radiogram obtained by a conventional molybdenum x-ray tube for mammography, using the filter, with a tube voltage of 25 kV and the same distance between the x-ray source and the imaging plate.

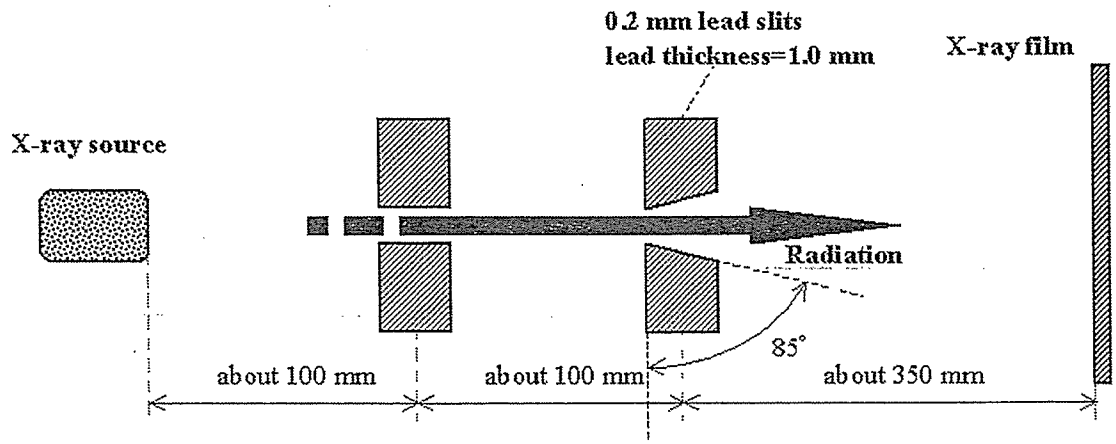

Fig. 9. Experimental setup for measuring x-ray divergence using two lead slits.

4.2 Image resolution and applications

Firstly, rough measurements of image resolution were made using wires. Figure 12 shows radiograms of tungsten wires coiled around rods made of PMMA with a charging voltage of 50 kV. Although the image contrast increased with increases in the wire diameter, a 50μm-diameter wire could be observed.

The image of water droplets falling into a polypropylene beaker from an injector is shown in Fig. 13. This image was taken with a charging voltage of 45 kV, with the slight addition of an iodine-based contrast medium. Because the x-ray duration was about 1μs, the stop-motion image of water could be obtained.

Figure 14 shows an angiogram of the external ear of a rabbit; iodine-based microspheres of 20μm diameter were used with a charging voltage of 45 kV, and fine blood vessels of about 50μm were clearly visible. In angiography of an extracted rabbit heart using iodine spheres with a voltage of 55 kV, fine coronary arteries were observed in the enlarged image (Fig. 15).

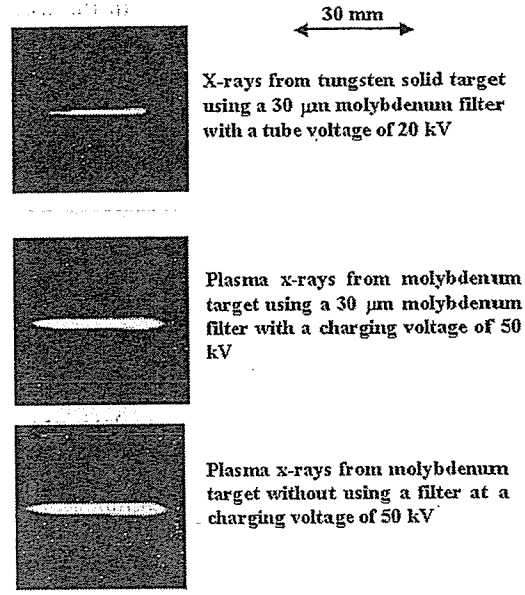

Fig. 10. X-ray divergence with two lead slits.

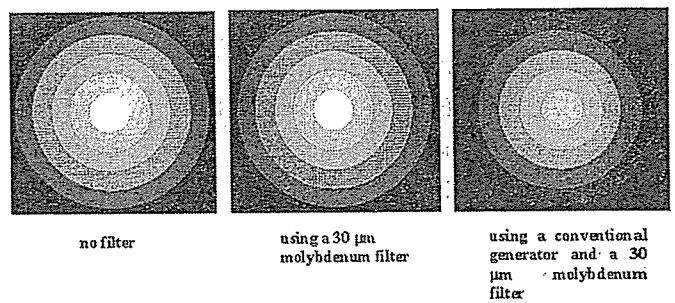

Fig. 11. Radiograms of concentric-circled steps of 5.0 mm with a maximum height of 25.0 mm at the indicated conditions.

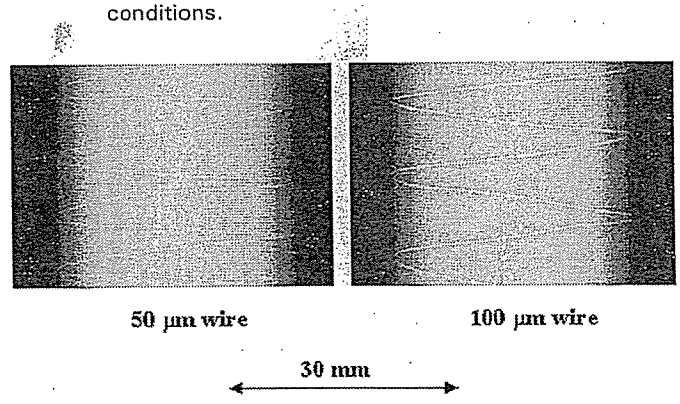

Fig. 12. Radiograms of tungsten wires of 50 and 100μm in diameter coiled around rods made of polymethyl methacrylate.

5. Discussion

Concerning the spectrum measurement, we obtained quite intense and sharp K-series lines by forming a weakly ionized linear plasma x-ray source. In fact, these rays penetrated the molybdenum filter easily and were diffused after passing through slits, with the average linear absorption coefficient slightly larger than that for quasi-monochromatic x-rays

from the solid molybdenum target. In the former experiment concerning the slit divergence, the radiations from linear plasma formed by a capillary were also diffused greatly as compared with incoherent visible light beams[21].

In this research, we obtained sufficient characteristic x-ray intensity per pulse for CR radiography without using a monochromatic filter, and the generator produced high-dose-rate quasi-monochromatic x-rays in a quantity roughly 1,000 times greater than the synchrotron monochromatic x-rays. In addition, since the photon energy of characteristic x-rays can be controlled by changing target elements, various quasi-monochromatic high-speed radiographies, such as high-contrast micro angiography[22] and parallel radiography[23] using an x-ray lens, will be possible.

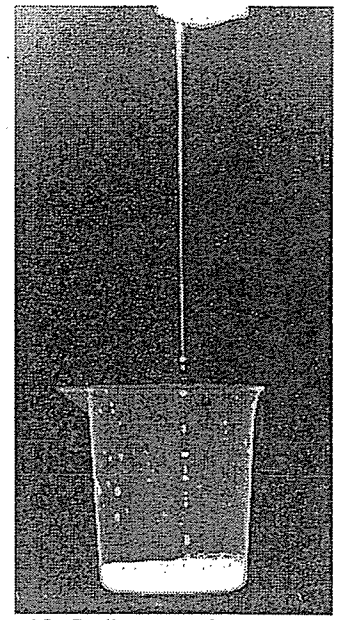

Fig. 13. Radiogram of water droplets falling into a polypropylene beaker from an injector.

Acknowledgment

This work was supported by Grants-in-Aid for Scientific Research from MECSST (12670902, 13470154, and 13877114), Grants from JST (Test of Fostering Potential), NEDO, and MHLW (HLSRG, RAMT-nano-001, RHGTEFB-genome-005, and RGCD13C-1).

References

1) Mattsson A: Some characteristics of a 600 kV flash x-ray tube. Physica Scripta 5: 99-102, 1972

2) Germer R: X-ray flash techniques. J Phys E: Sci Instrum 12: 336-350, 1979

3) Sato E, Kimura S, Kawasaki S, et al.: Repetitive flash x-ray generator utilizing a simple diode with a new type of energy-selective function. Rev Sci Instrum 61: 2343-2348, 1990

4) Sato E, Isobe H, Hoshino F: High intensity flash x-ray apparatus for biomedical radiography. Rev Sci Instrum 57: 1399-1408, 1986

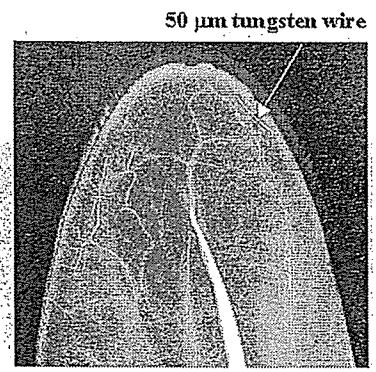

Fig. 14. Angiograms of the external ear of a rabbit.

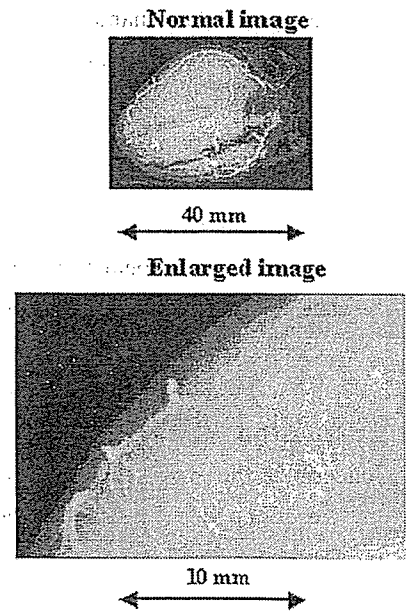

Fig. 15. Angiograms of an extracted rabbit heart.

5) Sato E, Shikoda A, Kimura S, et al.: Repetitive compact flash x-ray generators for soft radiography. SPIE 1801: 628-642, 1992
6) Kimura S, Sato E, Sagae M, et al.: Disk-cathode flash x-ray tube driven by a repetitive two-stage Marx pulser. Med & Biol Eng & Comput 31: S37-S43, 1993
7) Sato E, Sagae M, Takahashi K, et al.: High-speed soft x-ray generators in biomedicine. SPIE 2513: 649-667, 1994
8) Sato E, Sagae M, Takahashi K, et al.: Dual energy flash x-ray generator. SPIE 2513: 723-735, 1994
9) Shikoda A, Sato E, Sagae M, et al.: Repetitive flash x-ray generator having a high-durability diode driven by a two-cable-type line pulser. Rev Sci Instrum 65: 850-856, 1994
10) Sato E, Takahashi K, Sagae M, et al.: Sub-kilohertz flash x-ray generator utilizing a glass-enclosed cold-cathode triode. Med & Biol Eng & Comput 32: 289-294, 1994
11) Takahashi K, Sato E, Sagae M, et al.: Fundamental study on a long-duration flash x-ray generator with a surface-discharge triode. Jpn J Appl Phys 33: 4146-4151, 1994
12) Sato E, Sagae M, Shikoda A, et al.: High-speed soft x-ray techniques. SPIE 2869: 937-955, 1996
13) Rocca JJ, Shlyaptsev V, Tomasel FG, et al.: Demonstration of a discharge pumped table-top soft x-ray laser. Phys Lev Lett 73: 2192-2195, 1994
14) Collins GP: Tabletop capillary-discharge soft-x-ray laser demonstrated. Physics Today Oct: 19-21, 1994
15) Rocca JJG, Chilla JLA, Sakadzic S, et al.: Advances in capillary discharge soft x-ray laser research. SPIE 4505: 1-6, 2001
16) Le Pape S, Zeitoun Ph, Rocca JJG, et al.: Characterisation of an x-ray laser beam. SPIE 4505: 23-34, 2001
17) Nakamori N, Yamano K, Yamada M, et al.: Calculation of characteristic x-rays in diagnostic x-ray spectrum. Jpn J Appl Phys 33: 347-352, 1994
18) Sato E, Sagae M, Ichimaru T, et al.: Tentative study on x-ray enhancement by fluorescent emission of radiation by plasma x-ray source. SPIE 3771: 51-60, 1999
19) Sato E, Hayashi Y, Ichimaru T, et al.: Tentative study on high-photon-energy quasi-x-ray laser generator by forming plasma x-ray source. SPIE 4183: 326-338, 2000
20) Sato E, Sato K, Tamakawa Y, et al.: Film-less computed radiography system for high-speed Imaging. Ann Rep Iwate Med Univ Sch Lib Arts & Sci 35: 13-23, 2000
21) Sato E, Hayashi Y, Usuki T, et al.: Characteristics of a capillary-discharge flash x-ray generator. SPIE 4786: 173-182, 2002
22) Mori H, Hyodo K, Tanaka E, et al.: Small-vessel radiography in situ with monochromatic synchrotron radiation. Radiology 201: 173-177, 1996
23) Sato E, Komatsu M, Hayashi Y, et al.: Quasi-monochromatic parallel radiography achieved with a plane-focus x-ray tube. SPIE 4786: 151-161, 2002

Annual Report of Iwate Medical University
School of Liberal Arts and Sciences
No. 38(2003), 23 - 29.

Development of an extremely soft x-ray generator

Eiichi Sato[a], Fumiko Obata[b], Kiyomi Takahashi[b], Shigehiro Sato[b], Etsuro Tanaka[c], Hidezo Mori[d], Toshiaki Kawai[e], Toshio Ichimaru[f], Kazuyoshi Takayama[g] and Hideaki Ido[h]

(Received October 17, 2003)

Abstract

The development of an extremely soft x-ray generator with a tungsten-target tube and its applications including radiography are described. This generator consists of a high-voltage transformer, a filament power supply, and an x-ray tube. Negative high voltages are applied to the cathode electrode in the x-ray tube, and the tube voltage and current are regulated by the input voltage of the transformer and the filament voltage, respectively. The x-ray tube is a glass-enclosed double-focus diode with a tungsten target and a 0.2 mm-thick beryllium window. The maximum tube voltage and the electric power were 60 kV and 400 W, respectively. The focal-spot sizes were 4 × 4 (large) and 1 × 1 mm (small), respectively. Radiography was performed with a computed radiography system. In angiography using iodine-based microspheres, we observed fine blood vessels of about 50 μm or less with high contrasts. Using this generator, we designed an experimental setup for disinfection achieved with extremely soft x rays.

Keywords: extremely soft x-ray, beryllium window, disinfection, soft radiography

1. Introduction

Synchrotrons generate high-dose-rate bremsstrahlung x rays with wide photon energy latitudes, and monochromatic x rays have been produced using single crystals. These monochromatic rays play an important role in parallel radiography and have been employed to perform high-contrast micro-angiography[1] and phase imaging.[2-4]

So far, several different flash x-ray generators have been developed, and soft generators[5-12] with photon

[a] Department of Physics, Iwate Medical University, 3-16-1 Honchodori, Morioka 020-0015, Japan
[b] Department of Microbiology, School of Medicine, Iwate Medical University, 19-1 Uchimaru, Morioka 020-8505, Japan
[c] Department of Nutritional Science, Faculty of Applied Bio-science, Tokyo University of Agriculture, 1-1-1 Sakuragaoka, Setagaya-ku 156-8502, Japan
[d] Department of Cardiac Physiology, National Cardiovascular Center Research Institute, 5-7-1 Fujishirodai, Suita, Osaka 565-8565, Japan
[e] Electron Tube Division #2, Hamamatsu Photonics Inc., 314-5 Shimokanzo, Toyooka Village, Iwata-gun 438-0193, Japan
[f] Department of Radiological Technology, School of Health Sciences, Hirosaki University, 66-1 Honcho, Hirosaki 036-8564, Japan
[g] Shock Wave Research Center, Institute of Fluid Science, Tohoku University, 2-1-1 Katahira, Aoba-ku, Sendai 980-8577, Japan
[h] Department of Applied Physics and Informatics, Faculty of Engineering, Tohoku Gakuin University, 1-13-1 Chuo, Tagajo 985-8537, Japan

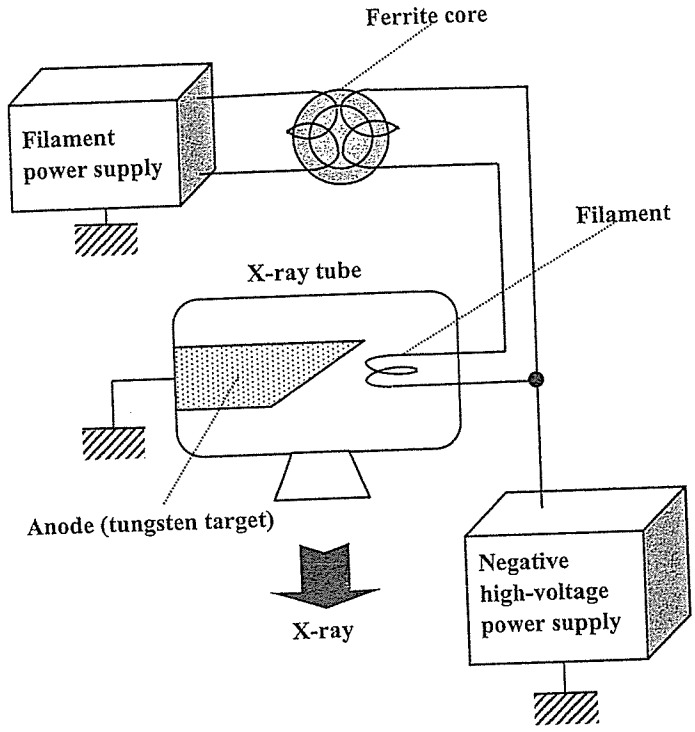

Fig. 1: Block diagram of the extremely soft x-ray generator.

energies of lower than 150 keV can be employed to perform biomedical radiography. In order to produce monochromatic x rays, plasma flash x-ray generators[13-18] are useful, since quite intense and sharp characteristic x rays such as lasers have been produced from weakly ionized linear plasmas of nickel, copper and molybdenum, while bremsstrahlung rays are hardly detected at all.
Currently, soft x rays are employed in order to perform soft radiographies with biomedical applications, and are fairly useful to image soft-tissue biomedical objects. Hereafter, the thickness of the x-ray window of the tube should be decreased as much as possible to produce soft bremsstrahlung x rays of lower than 5 keV. In addition, soft x rays may be used to perform disinfection of various fungi including anthrax, because the x rays are absorbed easily by fungi.
In the present research, we developed an extremely soft x-ray generator with a tungsten-target tube, and used it to perform preliminary studies on disinfection and extremely soft radiography.

2. Generator

Figure 1 shows the block diagram of the x-ray generator, which consists of a high voltage power supply (Figs. 2 and 3), an x-ray tube unit (Fig. 4), and a filament power supply (Fig. 5). The negative high-voltage is applied to the cathode electrode, and the anode (target) is connected to the ground potential. In this experiment, the peak tube voltage was regulated from 10 to 15 kV, and the peak tube current was regulated within 15 mA by the filament voltage (temperature). The exposure time is controlled in

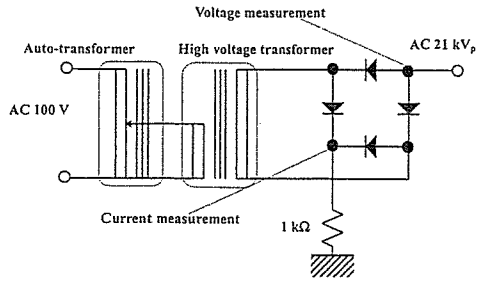

Fig. 2: Circuit diagram of the high voltage power supply.

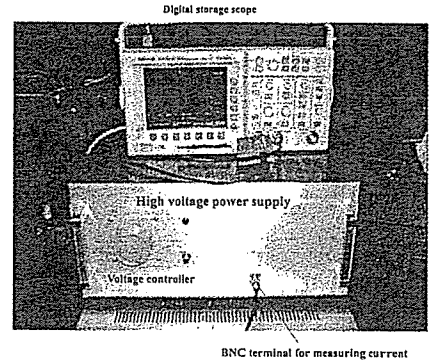

Fig. 3: High-voltage power supply.

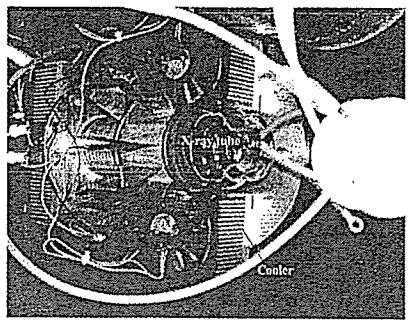

Fig. 4: X-ray tube unit with coolers.

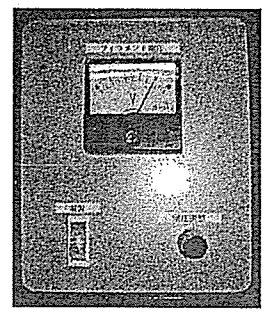

Fig. 5: Filament power supply.

order to obtain optimum x-ray intensity, and the x-ray tube is a double-focus type with focal-spot dimensions of approximately 4 × 4 (large spot) and 1 × 1 mm (small spot), respectively.

3. Characteristics

3.1. Cathode voltage and current

The tube voltage and current were measured by a high-voltage divider and a resistor, respectively, and the tube voltage was −1 times the cathode voltage. Figure 6 shows variations in the voltage and current. At a constant filament voltage of 8 V, the peak tube current increased with increases in the voltage. Next, at a constant tube voltage, the peak current increased when the filament voltage was increased.

3.2. X-ray source

In order to measure images of the x-ray source, we employed a pinhole camera with a hole diameter of 50 μm in conjunction with a Computed Radiography (CR) system.[19] The dimensions of small and large spots seldom varied and had values of approximately 1 × 1 and 4 × 4 mm, respectively.

3.3. X-ray spectra

Figure 7 shows transmittivities of beryllium and dry air with changes in the photon energy. When a 0.2 mm-thick beryllium window is employed, x-ray spectra with energies of lower than 2 keV are absorbed

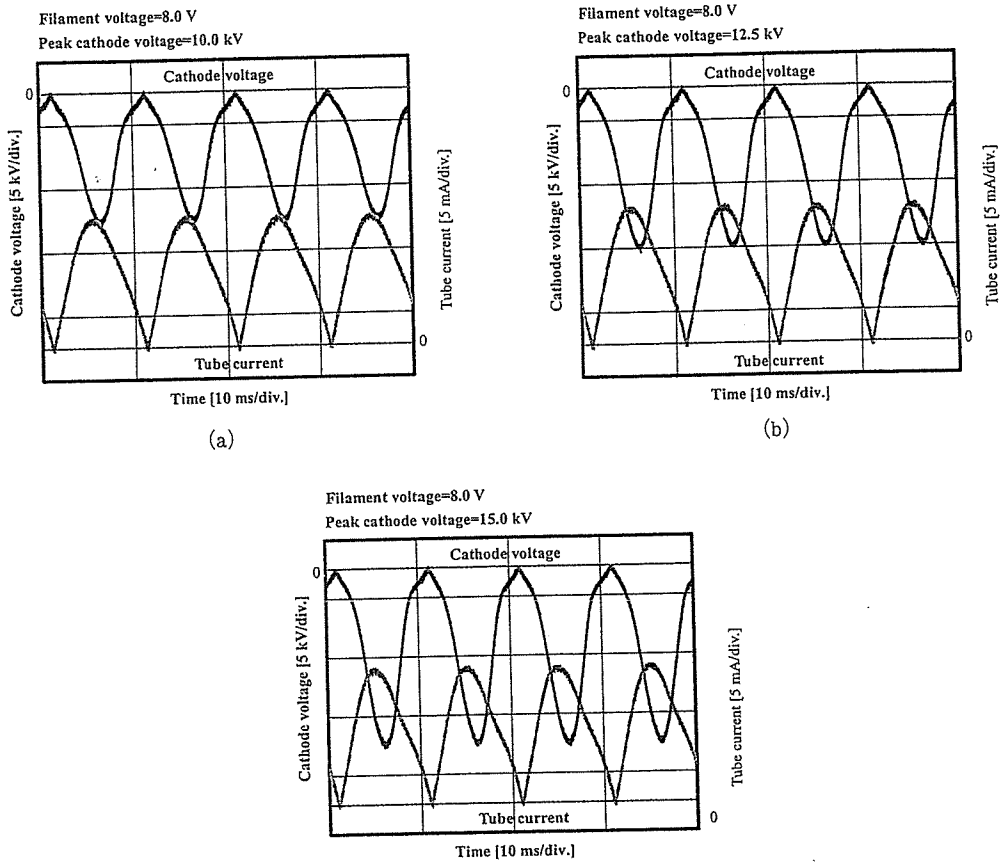

Fig. 6: Cathode voltages and tube currents at the indicated conditions.

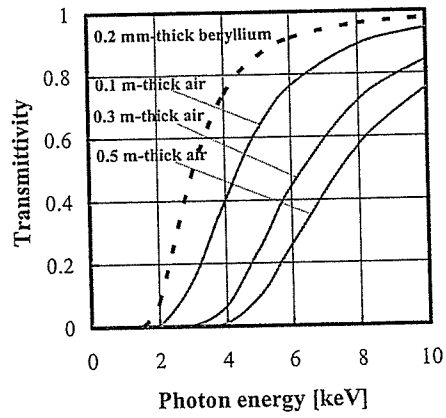

Fig. 7: Transmittivities of x rays with the photon energy.

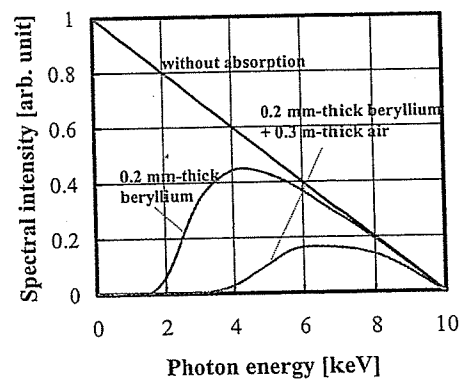

Fig. 8: Calculated bremsstrahlung spectra at the indicated conditions.

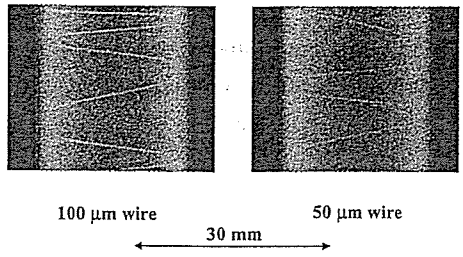

Fig. 9: Radiograms of tungsten wires of 50 and 100 μm in diameter coiled around pipes made of polymethyl methacrylate.

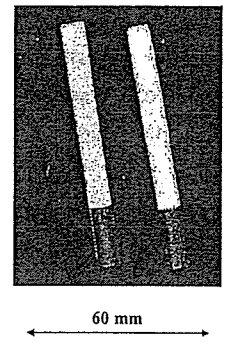

Fig. 10: Radiogram of cigarettes.

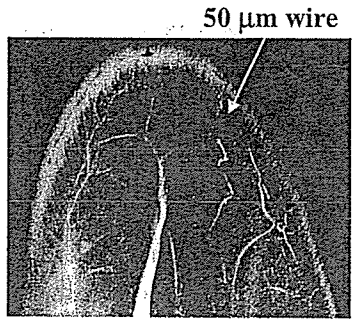

Fig. 11: Angiograms of the external ear of a rabbit using iodine-based microspheres.

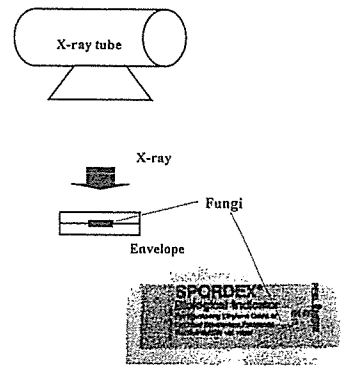

Fig. 12: Experimental setup for disinfection.

effectively. Subsequently, 0.5 m-thick air transmits x rays with energies of higher than 4 keV.
The x-ray spectra were calculated by the mass attenuation coefficients of the beryllium and the dry air (Fig. 8). As shown in this figure, the soft x rays of lower than 2 keV were primarily absorbed by the beryllium x-ray window, and the rays were also absorbed by the air. Therefore, the distance should be decreased as much as possible in order to obtain soft x rays.

4. Radiography

The radiography was performed by the CR system (Konica Regius 150), and the distance between the x-ray source and imaging plate was 0.35 m. Next, the peak tube voltage, the peak current, and the exposure time were 10 kV, 10 mA, and 10 s, respectively. Figure 9 shows radiograms of tungsten wires coiled around pipes made of polymethyl methacrylate. Although the image contrast increased with increases in the wire diameter, a 50 μm-diameter wire could be observed.
A radiogram of cigarettes is shown in Fig. 10. In this radiography, we obtained an extremely soft radiogram, and the contents of cigarettes were hardly observed at all.
Figure 11 shows an angiogram of the external ear of a rabbit; iodine-based microspheres of 15 μm diameter were used, and fine blood vessels of about 50 μm were clearly visible.

5. Design of experimental setup for disinfection

Figure 12 shows the experimental setup for disinfection using soft x rays. Fungi were enclosed in an envelope and were exposed to soft x rays. After measuring all the radiographic characteristics, we plan to perform disinfection of various fungi with changes in the radiographic conditions.

6. Discussion

In the present work, we succeeded in generating extremely soft x rays using a 0.2 mm-thick beryllium window in conjunction with a tungsten target. Therefore, L-series characteristic x rays are produced with tube voltage of higher than 12.1 kV. In radiography, the image quality became hard according to increases in the thickness of the aluminum filter, because the low photon energy x rays were absorbed easily by the filter. Using this x-ray generator, although K-series characteristic x rays of tungsten are not produced due to the tube voltage, the photon energies of the characteristic x rays can be selected by the target element.

In disinfection, the distance between the x-ray source and fungi should be decreased as much as possible to decrease the absorbed x-ray intensity by air. Subsequently, because the air is dissociated greatly, ion beams will also be a useful technique for disinfection and the excluding of static electricity from semiconductor devices.

Because it is possible to produce low photon energy x rays and to perform extremely soft radiography and x-ray disinfection, and to exclude electricity, this system can be applied in various fields.

Acknowledgments

This work was supported by Grants-in-Aid for Scientific Research and Advanced Medical Scientific Research from MECSST (12670902, 13470154, and 13877114), Grants from Keiryo Research Foundation, JST (Test of Fostering Potential), NEDO, and MHLW (HLSRG, RAMT-nano-001, RHGTEFB-genome-005, and RGCD13C-1).

References

1. H. Mori, K. Hyodo, E. Tanaka, M.U. Mohammed, A. Yamakawa, Y. Shinozaki, H. Nakazawa, Y. Tanaka, T. Sekka, Y. Iwata, S. Honda, K. Umetani, H. Ueki, T. Yokoyama, K. Tanioka, M. Kubota, H. Hosaka, N. Ishizawa and M. Ando, "Small-vessel radiography in situ with monochromatic synchrotoron radiation," *Radiology*, **201**, pp. 173-177, 1996.
2. T.J. Davis, D. Gao, T.E. Gureyev, A.W. Stevenson and S.W. Wilkims, "Phase-contrast imagimg of weakly absorbing materials using hard x-rays," *Nature*, **373**, pp. 595-597, 1995.
3. A. Momose, T. Takeda, Y. Itai and K. Hirano, "Phase-contrast x-ray computed tomography for observing biological soft tissues," *Nature Medicine*, **2(4)**, pp. 473-475, 1996.
4. A. Ishisaka, H. Ohara and C. Honda, "A new method of analyzing edge effect in phase contrast imaging with incoherent x-rays," *Opt. Rev*, **7**, pp. 566-572, 2000.
5. E. Sato, S. Kimura, S. Kawasaki, H. Isobe, K. Takahashi, Y. Tamakawa and T. Yanagisawa, "Repetitive flash x-ray generator utilizing a simple diode with a new type of energy-selective function," *Rev. Sci. Instrum.*, **61**, pp. 2343-2348, 1990.
6. S. Kimura, E. Sato, M. Sagae, A. Shikoda, T. Oizumi, K. Takahashi, Y. Tamakawa and T. Yanagisawa,

"Disk-cathode flash x-ray tube driven by a repetitive two-stage Marx pulser," *Med. & Biol. Eng. & Comput.*, **31**, pp. S37-S43, 1993.

7. E. Sato, M. Sagae, K. Takahashi, T. Oizumi, H. Ojima, K. Takayama, Y. Tamakawa, T. Yanagisawa, A. Fujiwara and K. Mitoya, "High-speed soft x-ray generators in biomedicine," *SPIE*, **2513**, pp. 649-667, 1994.
8. E. Sato, M. Sagae, K. Takahashi, A. Shikoda, T. Oizumi, H. Ojima, K. Takayama, Y. Tamakawa, T. Yanagisawa, A. Fujiwara and K. Mitoya, "Dual energy flash x-ray generator," *SPIE*, **2513**, pp. 723-735, 1994.
9. A. Shikoda, E. Sato, M. Sagae, T. Oizumi, Y. Tamakawa and T. Yanagisawa, "Repetitive flash x-ray generator having a high-durability diode driven by a two-cable-type line pulser," *Rev. Sci. Instrum.*, **65**, pp. 850-856, 1994.
10. E. Sato, K. Takahashi, M. Sagae, S. Kimura, T. Oizumi, Y. Hayasi, Y. Tamakawa and T. Yanagisawa, "Sub-kilohertz flash x-ray generator utilizing a glass-enclosed cold-cathode triode," *Med. & Biol. Eng. & Comput.*, **32**, pp. 289-294, 1994.
11. K. Takahashi, E. Sato, M. Sagae, T. Oizumi, Y. Tamakawa and T. Yanagisawa, "Fundamental study on a long-duration flash x-ray generator with a surface-discharge triode," *Jpn. J. Appl. Phys.*, **33**, pp. 4146-4151, 1994.
12. E. Sato, M. Sagae, A. Shikoda, K. Takahashi, T. Oizumi, M. Yamamoto, A. Takabe, K. Sakamaki, Y. Hayasi, H. Ojima, K. Takayama and Y. Tamakawa, "High-speed soft x-ray techniques," *SPIE*, **2869**, pp. 937-955, 1996.
13. E. Sato, Y. Suzuki, Y. Hayasi, E. Tanaka, H. Mori, T. Kawai, K. Takayama, H. Ido and Y. Tamakawa, "High-intensity quasi-monochromatic x-ray irradiation from the linear plasma target," *SPIE*, **4505**, pp. 154-164, 2001.
14. E. Sato, Y. Hayasi, E. Tanaka, H. Mori, T. Kawai, H. Obara, T. Ichimaru, K. Takayama, H. Ido, T. Usuki, K. Sato and Y. Tamakawa, "Polycapillary radiography using a quasi-x-ray laser generator," *SPIE*, **4508**, pp. 176-187, 2001.
15. E. Sato, Y. Hayasi, E. Tanaka, H. Mori, T. Kawai, T. Usuki, K. Sato, H. Obara, T. Ichimaru, K. Takayama, H. Ido and Y. Tamakawa, "Quasi-monochromatic radiography using a high-intensity quasi-x-ray laser generator," *SPIE*, **4682**, pp. 538-548, 2002.
16. E. Sato, Y. Hayasi, R. Germer, E. Tanaka, H. Mori, T. Kawai, H. Obara, T. Ichimaru, K. Takayama and H. Ido, "Intense characteristic x-ray irradiation from weakly ionized linear plasma and applications," *Jpn. J. Med. Imag. Inform. Sci.*, **20**, pp. 148-155, 2003.
17. E. Sato, Y. Hayasi, R. Germer, E. Tanaka, H. Mori, T. Kawai, H. Obara, T. Ichimaru, K. Takayama and H. Ido, "Irradiation of intense characteristic x-rays from weakly ionized linear molybdenum plasma," *Jpn. J. Med. Phys.*, **20**, pp. 123-131, 2003.
18. E. Sato, Y. Hayasi, R. Germer, E. Tanaka, H. Mori, T. Kawai, T. Ichimaru, K. Takayama and Hideaki Ido, "Quasi-monochromatic flash x-ray generator utilizing weakly ionized linear copper plasma," *Rev. Sci. Instrum.*, **74**, pp. 5236-5240, 2003.
19. E. Sato, K. Sato and Y. Tamakawa, "Film-less computed radiography system for high-speed Imaging," *Ann. Rep. Iwate Med. Univ. Sch. Lib. Arts and Sci.*, **35**, pp. 13-23, 2000.

British Journal of Pharmacology (2003) 139, 899–910
www.nature.com/bjp

Changes in functional and histological distributions of nitric oxide synthase caused by chronic hypoxia in rat small pulmonary arteries

*,[1]Mikiyasu Shirai, [1]James T. Pearson, [1]Akito Shimouchi, [1]Noritoshi Nagaya, [1]Hirotsugu Tsuchimochi, [2]Ishio Ninomiya & [1]Hidezo Mori

[1]Department of Cardiac Physiology, National Cardiovascular Centre Research Institute, 5-7-1 Fujishiro-dai, Suita, Osaka 565-8565, Japan and [2]Department of Engineering, Faculty of Health Sciences, Hiroshima International University, Hiroshima 724-0695, Japan

1 Chronic hypoxia (CH) increases lung tissue expression of all types of nitric oxide synthase (NOS) in the rat. However, it remains unknown whether CH-induced changes in functional and histological NOS distributions are correlated in rat small pulmonary arteries.

2 We measured the effects of NOS inhibitors on the internal diameters (ID) of muscular (MPA) and elastic (EPA) pulmonary arteries (100–700 μm ID) using an X-ray television system on anaesthetized rats. We also conducted NOS immunohistochemical localization on the same vessels.

3 Nonselective NOS inhibitors induced ID reductions in almost all MPA of CH rats (mean reduction, 36±3%), as compared to ~60% of control rat MPA (mean, 10±2%). The inhibitors reduced the ID of almost all EPA with similar mean values (~26%) in both CH and control rats. On the other hand, inducible NOS (iNOS)-selective inhibitors caused ID reductions in ~60% of CH rat MPA (mean, 15±3%), but did so in only ~20% of control rat MPA (mean, 2±2%). This inhibition caused only a small reduction (mean, ~4%) in both CH and control rat EPA. A neuronal NOS-selective inhibitor had no effect.

4 The percentage of endothelial NOS (eNOS)-positive vessels was ~96% in both MPA and EPA from CH rats, whereas it was 51 and 91% in control MPA and EPA, respectively. The percentage for iNOS was ~60% in both MPA and EPA from CH rats, but was only ~8% in both arteries from control rats.

5 The data indicate that in CH rats, both functional and histological upregulation of eNOS extensively occurs within MPA. iNOS protein increases sporadically among parallel-arranged branches in both MPA and EPA, but its vasodilatory effect is predominantly observed in MPA. Such NOS upregulation may serve to attenuate hypoxic vasoconstriction, which occurs primarily in MPA and inhibit the progress of pulmonary hypertension.
British Journal of Pharmacology (2003) **139**, 899–910. doi:10.1038/sj.bjp.0705312

Keywords: Chronic hypoxia; pulmonary hypertension; small pulmonary arteries; endogenous NO; L-NAME; L-NMMA; L-canavanine; s-methylisothiourea; 7-nitro indazole; NOS immunohistochemistry

Abbreviations: CH, chronic hypoxia; GMP, guanosine-3′,5′-monophosphate; ID, internal diameter; LV, left ventricle; L-NAME, N^{ω}-nitro-L-arginine methyl ester; L-NMMA, N^{ω}-monomethyl-L-arginine; NO, nitric oxide; eNOS, endothelial NO synthase; iNOS, inducible NO synthase; nNOS, neuronal NO synthase; PAP, pulmonary arterial pressure; RV, right ventricle; SAP, systemic arterial pressure

Introduction

The change in lung expression of nitric oxide synthase (NOS) in response to chronic hypoxia (CH) has extensively been studied in the rat. Northern and Western blot analyses in hypoxic rats have demonstrated increased lung tissue expression of mRNA and protein for endothelial NOS (eNOS) (Xue *et al.*, 1994; Shaul *et al.*, 1995; Le Cras *et al.*, 1996; 1998; Xue & Johns, 1996; Tyler *et al.*, 1999), inducible NOS (iNOS) (Xue *et al.*, 1994; Le Cras *et al.*, 1996; Xue & Johns, 1996), and neuronal NOS (nNOS) (Xue & Johns, 1996). The significant increases in gene and protein expression were observed as early as 24 h after hypoxia (Xue & Johns, 1996). NOS immunohistochemistry has shown that the hypoxic increase in eNOS staining intensity is induced in the pulmonary arteries (diameter 50–300 μm) but not in veins (60–300 μm) (Resta *et al.*, 1997). On the other hand, iNOS increased in vascular smooth muscle at all levels of hypoxic pulmonary vessels, although it was very limited in normoxic pulmonary vessels (Xue *et al.*, 1994; Xue & Johns, 1996). Moreover, the majority of nNOS immunoreactivity was distributed in bronchial epithelial cells, although it was found in the neurons surrounding the large bronchi (Xue & Johns, 1996).

The functional role of endogenous nitric oxide (NO) in modulating pulmonary vascular tone of the CH rat has been examined chiefly by use of isolated perfused lungs or isolated proximal elastic pulmonary arteries (main or extralobar pulmonary arteries). Most, but not all (Adnot *et al.*, 1991; Eddahibi *et al.*, 1992), pressure-flow studies of hypoxic lungs have suggested either normal or increased responsiveness to the nonselective NOS inhibitor (Barer *et al.*, 1993; Russ &

*Author for correspondence; E-mail: mshirai@ri.ncvc.go.jp

Walker, 1993; Isaacson *et al.*, 1994; Roos *et al.*, 1996; Muramatsu *et al.*, 1997; Tyler *et al.*, 1999) and to endothelium-dependent vasodilators (Barer *et al.*, 1993; Russ & Walker, 1993; Isaacson *et al.*, 1994; Muramatsu *et al.*, 1996; Resta & Walker, 1996; Roos *et al.*, 1996). In contrast, isolated proximal arteries have impaired responsiveness to endothelium-dependent vasodilators (Crawley *et al.*, 1992; Rodman, 1992; Carville *et al.*, 1993; Shaul *et al.*, 1993; Maruyama & Maruyama, 1994). These data suggest the possibility that the effect of CH on endogenous NO-mediated vasodilatation differs between the muscular (resistance) and elastic (conduit) pulmonary vessels in the rat. Recently, using a selective iNOS inhibitor, a pressure-flow study has suggested that NO derived from iNOS does not modulate pulmonary vasoconstrictor responsiveness in isolated lungs from CH rats (Resta *et al.*, 1999).

Despite such extensive structural and functional studies, the following problems have yet to be examined sufficiently in the CH rat. One issue is whether, and to what extent, the effect of hypoxia on the NO-mediated basal vascular tone regulation varies along the series-connected small pulmonary arteries, from elastic to muscular segment levels and, moreover, between the parallel-arranged vascular branches within each vascular segment level. Another is whether the increased iNOS and nNOS can contribute to the basal tone regulation in these small arteries. To resolve these issues, we applied a specially designed X-ray television system (Sada *et al.*, 1985; Shirai *et al.*, 1986) on anaesthetized rats and directly measured internal diameter (ID) changes due to NOS inhibition in the pulmonary arterial trees (100–700 μm ID), which contain both muscular and distal elastic segments (Kay, 1983; Sasaki *et al.*, 1995). We used the *in vivo* pulmonary circulation associated with natural blood perfusate and flow pattern, because these are important factors for determining the expression of NO activity (Hakim, 1994; Sprague *et al.*, 1995). The ID changes were compared between 4-week hypoxic rats and normoxic control rats. N^{ω}-nitro-L-arginine methyl ester (L-NAME) or N^{ω}-monomethyl-L-arginine (L-NMMA) was used for nonselective NOS inhibition, L-canavarine or *S*-methylisothiourea sulphate for selective inhibition of iNOS (Szabo *et al.*, 1994; Teale & Atkinson, 1994; Liaudet *et al.*, 1996) and 7-nitro indazole for selective inhibition of nNOS (Moore *et al.*, 1993; Kalisch *et al.*, 1996; Okamoto *et al.*, 1997). We found that nonselective NOS inhibition and iNOS-selective inhibition cause significant ID changes, but nNOS-selective inhibition does not. Therefore, after these physiological studies, we further analysed eNOS and iNOS immunohistochemical localization in the pulmonary arteries to examine the correspondence between the structural and functional upregulation of NOS.

Methods

The study was conducted in accordance with the Guiding Principles for the Care and Use of Animals in the Field of Physiological Sciences, published by the Physiological Society of Japan. Male Sprague–Dawley rats were used for all experiments.

Chronic environment

Rats aged 6 weeks at the start of the experiment were placed in either a normobaric environmental chamber maintained at 10% O_2 (hypoxic group, $n=15$) or a chamber open to room air (control normoxic group, $n=11$) for 4 weeks. Carbon dioxide was removed by self-indicating soda lime granules and excess humidity prevented by cooling of the recirculation circuit. The environment within the chamber was monitored with a mass spectrometer. All hypoxic and normoxic rats were kept in the same room, at the same light–dark cycle. Food and water were available *ad libitum*. The chamber was opened for ~10 min daily to clean the cages and replenish food and water.

Experimental procedure and angiography

Rats were anaesthetized with pentobarbital sodium (50 mg kg^{-1} i.p.) and supplemental doses (10–20 mg kg^{-1} h^{-1} i.v.) were administered to maintain an appropriate level of anaesthesia. Each rat was intubated with an endotracheal tube and artificially ventilated with room air. A *syrustic* catheter (outer diameter, ~500 μm) was introduced from the right jugular vein into the left main pulmonary artery. Another catheter was inserted into the right femoral artery. Thereafter, the left-side rib cage was partially excised to expose directly the left lung to the X-ray. The end-expiratory pressure was adjusted to 3.0 cm H_2O to prevent lung collapse. Heparin sodium (500 IU kg^{-1}) was administered to prevent blood coagulation.

The system and experimental set-up used in the angiography have been described previously in detail (Sada *et al.*, 1985; Shirai *et al.*, 1986). Briefly, the rat was placed inside an X-ray apparatus box (Hitex) and fixed in such a manner that the exposed left lobe automatically came into contact with a plate just above the beryllium faceplate of an X-ray-sensitive, 1-in. vidicon camera (Hamamatsu Photonics). During temporary cessation of ventilation for ~3 s at end expiration, a contrast medium (0.2 ml, 60% Urografin) was injected into the main pulmonary artery at a constant speed (0.15 ml s^{-1}), and its passage through the pulmonary vascular bed recorded serially at high speed (30 frames s^{-1}) on a videotape recorder (PVW-2800, Sony). During the experiment, the temperature in the box was maintained at 25–28°C, and the surface of the exposed lung kept wet by warm (37°C) saline. Blood gases and pH were examined by a blood gas analyzer (ABL-2, Radiometer).

ID measurement

The serial angiograms recorded on the videotape recorder were then transferred to a digital image processor (DVS-5000, Hamamatsu). To obtain the arteriogram for measuring ID, two to three serial frames within a diastolic phase, in which vascular trees were extensively filled with contrast medium, were added up and averaged by the digital image processor. The processed image was electrically transferred to an image hard copy unit (model 4634, Sony Tektronix) and copied clearly onto paper. The ID of the pulmonary vessels on the copy was then measured manually using a digitizer (model 9874A, Hewlett-Packard) connected to a minicomputer. The readers of the angiograms were blinded to the treatment protocol.

Analysis of ID response

Following the method we described in a previous study (Shirai *et al.*, 1986), we took a random selection of many vascular sites

for the ID measurements. The ID percentage change in response to an NOS inhibitor was calculated at each measured vascular site. These sites were classified into three vascular groups, that is the muscular arteries (100–300 μm ID), smaller transitional elastic arteries (400–500 μm), and larger classical elastic arteries (600–700 μm), according to their vascular branching pattern and baseline ID sizes (Kay, 1983; Sasaki *et al.*, 1995). By pooling all the data within a vascular group, the mean value of the ID percentage change was obtained in each of the three groups. The ID responses were separated into three types (constriction, dilatation, and no change) according to the following definition: an increase or decrease more than 5% in the percentage ID change is defined as dilatation or constriction, respectively, and a change below 5% as no change.

In the present study, the mean pulmonary arterial pressure (PAP) of the CH rat was ~3 mmHg larger than that of the control rat under baseline conditions, suggesting that the baseline ID at the same serial segments of arteries may differ between these rats. Therefore, we compared the baseline ID of primary branches (400–600 μm) arising from the axial artery or peripheral branches (<300 μm) arising from the primary branch (Sasaki *et al.*, 1995) between these rats. However, there was no significant difference in the mean baseline ID value at any of the serial segments.

Experimental protocols for angiography

In each of the hypoxic and normoxic groups, the baseline angiogram was recorded first, and then an injection of nonselective NOS inhibitor ($n=4$), L-NAME (50 mg kg^{-1} i.v., $n=2$) or L-NMMA (60 mg kg^{-1} i.v., $n=2$), an injection of iNOS selective inhibitor ($n=4$), L-canavanine (100 mg kg^{-1} i.v., $n=2$) or *S*-methylisothiourea sulphate (3 mg kg^{-1} i.v., $n=2$), or an injection of nNOS selective inhibitor, 7-nitro indazole (50 mg kg^{-1} i.p., $n=3$), was performed. The angiograms following the injection of a nonselective NOS inhibitor or an iNOS selective inhibitor were taken ~20 min after the injection ended. Similarly, the angiogram was recorded 30–40 min after the injection of an nNOS selective inhibitor. In our preliminary dose–response data, the doses of NOS inhibitors were enough to cause maximal levels of ID reduction. Moreover, the magnitudes and distribution patterns of the ID reduction caused by the two chemically different nonselective NOS inhibitors, as well as the two iNOS inhibitors, were similar. Therefore, we considered that nonspecific effects other than those due to NOS inhibition are negligibly small in the doses used in the present study and that pooling the data from the two different inhibitors is reasonable.

We found significant ID reductions after the injections of a nonselective NOS inhibitor and an iNOS selective inhibitor, but not after nNOS selective inhibitor injection. To examine whether these ID constrictions primarily resulted from inhibiting the release of NO derived from L-arginine, the third angiogram following the addition of L-arginine (100–200 mg kg^{-1} i.v.) was further recorded in the rats given a nonselective NOS inhibitor or an iNOS selective inhibitor.

In the current study, PAP increased by ~3 mmHg after the nonselective NOS inhibitor administration in the CH rat. It is thus possible that the pressure-sensing mechanism (see Discussion) influenced the ID change pattern in response to the inhibitor. To examine this possibility, we measured the effects of mechanically induced PAP increase on the ID of pulmonary arteries in CH rats ($n=4$). PAP was increased ~4 mmHg above the baseline value by partially interrupting blood flow into the right side of the lungs. The angiogram of the left lung was recorded at the time when the PAP increase was maintained for 50–60 s periods.

There was an interval of ~15 min between each angiography to eliminate any influence of the contrast medium. All experiments were finished within a few hours of removal from the chamber.

Immunohistochemistry and histology

Within the rats that had been used for recording angiograms with nonselective NOS inhibition and iNOS selective inhibition, immunolocalization of NOS proteins in the pulmonary arteries was performed. Four out of eight hypoxic rats and four out of eight normoxic rats were employed. After putting marks on the left lung regions, where the ID changes had been measured, the lungs were isolated from the rats under anaesthesia. Cannulas were inserted into the pulmonary artery and left atrium, and the lungs were perfused with heparinized phosphate-buffered saline (PBS) followed by 4% paraformaldehyde in 0.1 M PBS (pH 7.3). Simultaneously, the lungs were inflated via the trachea to a pressure of 23 cm H_2O with 4% paraformaldehyde and then placed in 10% buffered formaline for paraffin embedding. The left lung tissues that had been marked were cut into 7–9-mm sections. Paraffin sections 2 μm thick were mounted onto precleaned slides (Superfrost Plus; Fisher Scientific, Springfield, NJ, U.S.A.), dewaxed in 100% xylene, and then rehydrated in graded alcohol solutions. Throughout the protocol, slides were washed, as appropriate, in PBS. Antigen retrieval was performed by microwave treatment and proteinase K treatment for eNOS and iNOS immunostaining, respectively. Sections were treated with 0.3% H_2O_2 (30 min) to inhibit endogenous peroxidases and incubated with normal serum (30 min) to reduce nonspecific binding of secondary antibodies. Sections were then incubated at 4°C overnight with either of two anti-NOS antibodies: (1) a mouse monoclonal antibody raised against a peptide fragment of amino acids 1030–1209 of human eNOS (1:3000 dilution; Transduction Laboratories, Lexington, KY, U.S.A.) or (2) a rabbit polyclonal antibody raised against a synthetic peptide corresponding to amino-acid residues 1131–1144 (with one additional N-terminal cysteine) of mouse macrophage iNOS (1:3000 dilusion; Alexis Corporation, Lausen, Switzerland). The anti-eNOS antibody was characterized for use in Western blot analysis (identifying protein bands at 140 kDa for eNOS), and showed wide species reactivity, including reactivity with human and rat NOS (Transduction Laboratories). The anti-iNOS antibody was also characterized by Western blot (identifying a band at 130 kDa) and showed reactivity with human and rat NOS (Alexis Corporation). After washing off unbounded primary antibodies, sections were incubated with secondary biotinylated antibodies against mouse or rabbit (DAKO Co., Japan) (30 min), followed by incubation in avidin/biotin/horseradish peroxidase complex (DAKO Co., Japan) (30 min). Subsequently, peroxidase activity was visualized by incubation (3 min) with 0.05% 3,3′-diaminobenzidine (DAKO Co., Japan), which gives a brown reaction product. The reaction was stopped by washing with

water. The slides were then counterstained with Mayer's haematoxylin, dehydrated, and mounted. For negative control studies, slides were incubated with mouse IgG (for monoclonal antibodies) or rabbit IgG (for polyclonal antibodies) instead of primary antibody. No staining was observed in these negative control sections. Serial sections were stained with elastic Van Gieson's method to distinguish arteries and veins by the presence of an internal elastic lamina (Resta *et al.*, 1997).

According to the classification proposed by Sakai *et al.*, the elastic and muscular arteries were distinguished by the structure of the media. Vessel diameters were calculated from their external circumference. Oblique sections in which the elastic laminae were indistinct at one or more points on the circumference were excluded from analysis. Slides were examined independently by three blinded reviewers and vessels counted for NOS-positive or NOS-negative staining.

Statistical methods

The significance of differences in ID values and haemodynamic data between the conditions of baseline and NOS inhibition (among the values of baseline, NOS inhibitor alone, and NOS inhibitor + L-arginine) was tested by a paired *t*-test (analysis of variance (ANOVA) and Scheffe's test). The differences in the ID and haemodynamic data between control and hypoxic groups were examined by an unpaired *t*-test. ID response differences among the different serial vascular segments were assessed by analysis of variance (ANOVA) and Scheffe's test. All data are expressed as mean ± s.e.m., and $P<0.05$ was considered significant.

Results

Baseline values of body and right ventricle (RV) and left ventricle weight, and blood gases in control and CH rats

The mean values of body weight, (right ventricle (RV)/left ventricle (LV) + septum) ratio, and systemic arterial blood P_{O_2}(Pa_{O_2}), P_{CO_2}(Pa_{CO_2}) and pH are compared between the control and CH rats (Table 1). Blood gases were measured during normoxic ventilation. Final body weight was ~30 g smaller in the CH rat than in the control rat, while RV/(LV + septum) ratio ~0.30 larger. There were no significant differences in blood gases between these rats.

Haemodynamic responses due to NOS inhibition

Mean PAP and mean systemic arterial pressure (SAP), before and after NOS inhibitor injection, are compared between the control and CH rats (Table 2). These parameters were measured just before injection of the contrast medium under normoxic ventilation. In the CH rat, the nonselective NOS inhibitors significantly increased PAP and SAP by 3.2 and 34 mmHg, respectively. In the normoxic rat, these inhibitors caused a significant increase (30 mmHg) only in SAP. In contrast, the iNOS and nNOS selective inhibitors significantly changed neither PAP nor SAP in both control and CH rats.

Table 1 Baseline values of body weight, RV/(LV + septum) weight ratio, and blood gases during normoxic ventilation

Parameters	*Control rats (n = 11)*	*4-wk hypoxia rats (n = 11)*
Initial body weight (g)	197 ± 2	196 ± 2
Final body weight (g)	327 ± 7	299 ± 5*
RV/(LV + septum) ratio	0.33 ± 0.03	0.62 ± 0.05**
pH	7.41 ± 0.02	7.37 ± 0.04
PO_2 (Torr)	96 ± 6	93 ± 5
PCO_2 (Torr)	33 ± 2	35 ± 2

Values are mean ± s.e.m. *$P<0.05$; **$P<0.01$ vs control rats.

Table 2 Mean pulmonary arterial pressure (PAP) and systemic arterial pressure (SAP) before and after NOS inhibitor injection

Blood pressure (mmHg)	*Control rats*	*4-week hypoxia rats*
(1) *Nonselective NOS inhibition (NNI)*		
PAP (baseline)	18.0 ± 0.5	21.1 ± 1.0*
PAP with NNI	18.6 ± 0.6	24.3 ± 1.1*, **
PAP with NNI + L-arginine	17.9 ± 0.6	23.3 ± 1.2*
SAP (baseline)	93 ± 6	101 ± 7
SAP with NNI	123 ± 7**	135 ± 9**
SAP with NNI + L-arginine	98 ± 7	108 ± 9
(2) *iNOS selective inhibition (ISI)*		
PAP (baseline)	17.2 ± 0.6	22.1 ± 1.1*
PAP with ISI	17.4 ± 0.7	22.9 ± 1.1*
PAP with ISI + L-arginine	17.1 ± 0.7	22.2 ± 1.1*
SAP (baseline)	96 ± 6	105 ± 7
SAP with ISI	98 ± 6	113 ± 8
SAP with ISI + L-arginine	94 ± 7	107 ± 8
(3) *nNOS selective inhibition (NSI)*		
PAP (baseline)	18.0 ± 0.5	22.4 ± 1.0*
PAP with NSI	18.2 ± 0.5	22.6 ± 1.0*
SAP (baseline)	94 ± 6	102 ± 7
SAP with NSI	96 ± 6	105 ± 7

Values are mean + s.e.m. The mean value in classes 1 and 2 was obtained by pooling all the data in response to two different nonselective NOS inhibitors and two iNOS-selective inhibitors, respectively. *$P<0.05$ vs control rats. **$P<0.05$ vs baseline.

Regional changes in NOS-inhibitor induced responses in parallel- and series-arranged pulmonary arteries following 4-week hypoxia

Figure 1 shows typical ID changes of small pulmonary arteries in response to L-NMMA injection in the control and CH rats. On injection, slight ID decreases were induced in the control rat. In the CH rat, in contrast, clear ID decreases occurred in many branches, particularly smaller branches.

The mean value of the NOS inhibitor-induced ID change at each level of the muscular, transitional elastic, and classical elastic arteries is shown in the control and CH rats (Figure 2). During nonselective NOS inhibition (left), the ID of all these arteries significantly constricted in both control and CH rats. The ID constriction of the muscular arteries was significantly ($P<0.05$) smaller than those of the transitional and classical elastic arteries in the control rat. Comparing the ID constric-

tion due to nonselective NOS inhibition between the control and CH rats, there was a large difference in the muscular arteries and a small but significant difference in the transitional elastic arteries, whereas no significant difference was present in the classical elastic arteries. On the other hand, during iNOS selective inhibition (right), no significant ID response was induced in any of the arteries in the control rat. However, in the CH rat, a significant ID constriction occurred locally in the muscular arteries. Therefore, a significant difference between the control and CH rats was restricted in these arteries. During nNOS selective inhibition, no significant ID response was observed at any of the muscular and elastic arteries in the control and CH rats. The mean values of ID changes for the muscular, transitional elastic, and classical elastic arteries of the control rat were 0 ± 2, 2 ± 2, and $1\pm2\%$, respectively, and those of the CH rat were 3 ± 2, 1 ± 2, and $3\pm2\%$, respectively.

After making an L-arginine injection, the ID decreases due to nonselective NOS inhibition and iNOS selective inhibition were completely abolished in both control and CH rats. The mean values of ID percentage changes in response to nonselective NOS inhibitor + L-arginine in the muscular, transitional elastic, and classical elastic arteries were -2 ± 4, 2 ± 4, and $4\pm3\%$, respectively, in the control rat, and were -3 ± 4, -1 ± 4, and $2\pm4\%$ for the CH rat, respectively. The mean values of ID percentage changes in response to iNOS selective inhibitor + L-arginine in the three levels of vessels were 3 ± 4, 4 ± 4, and $1\pm4\%$, respectively, in the control rat, and were 1 ± 4, 3 ± 4, and $-2\pm4\%$ for the CH rat, respectively.

Relative frequency distribution of ID response due to NOS inhibition is compared between the control and CH rats (Figure 3). During nonselective NOS inhibition (left panels), the frequency curves of the control and CH rats were very different in the muscular arteries (100–300 μm), but not in the transitional (400–500 μm) and classical (600–700 μm) elastic arteries. In the muscular arteries, the peaks of the control and CH curves were observed at 5–15 and 35–45% constriction, respectively. Moreover, ~40% of ID responses were no change in the control vessels, but almost all ID responses were significant constriction in the CH vessels. In the transitional and classical elastic arteries, almost all ID responses were significant constriction in both control and CH vessels. The peaks of the control and CH distributions in the transitional arteries were at 15–25 and 25–35% constriction, respectively, but those for classical arteries were about the same level (25–35% constriction).

During iNOS selective inhibition (right panels), a clear difference between the control and CH response distributions existed only in the muscular arteries. In these arteries, the peaks of the control and CH curves were observed at no change and 5–15% constriction, respectively. Significant constriction was only ~20% of the ID responses in the control distribution, but ~60% in the CH. However, it is noteworthy that, in contrast to the case of nonselective NOS inhibition, ~40% of muscular artery responses were still no change in the CH rat. In the elastic arteries, just as in the muscular arteries, ~80% of the ID responses in the control distribution curve were no change, and the curves of the control and CH rats displayed similar patterns.

During nNOS selective inhibition, more than 95% of the ID responses were no change and the remaining responses, if any, were small constrictions in both the control and CH rats.

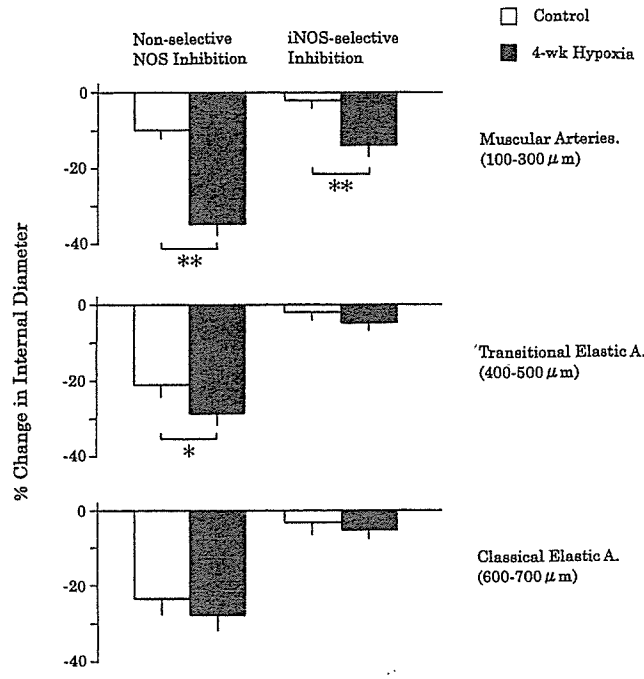

Figure 2 Mean values of NOS inhibitor-induced ID changes for muscular, transitional elastic, and classical elastic pulmonary arteries are shown in control (open column) and chronically hypoxic (solid column) rats. CH greatly enhanced ID reductions due to nonselective NOS inhibition (left) and iNOS-selective inhibition (right) primarily in muscular pulmonary arteries. $^*P<0.05$, $^{**}P<0.01$ vs control.

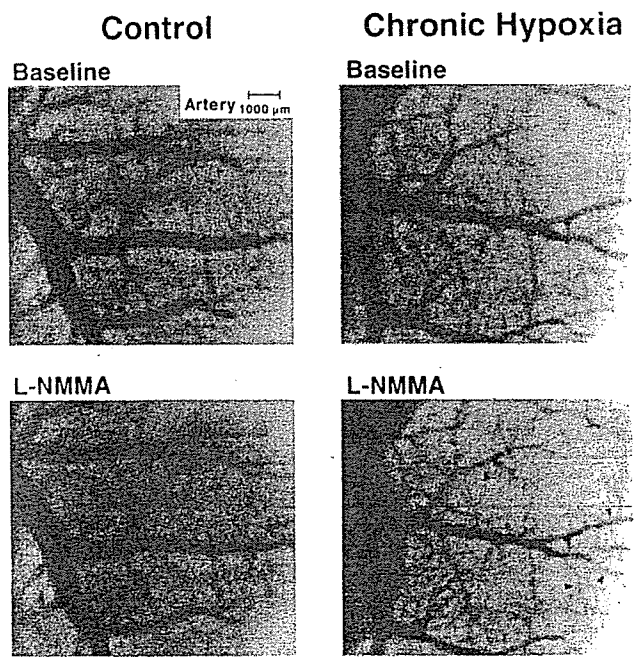

Figure 1 Typical angiograms of small pulmonary arteries obtained before (top panels) and after (bottom panels) nonselective NOS inhibitor (L-NMMA) injection in control (left panels) and chronically hypoxic (right panels) rats. Clear vasoconstrictions are chiefly observed in more distal side vessels $\lesssim 300\,\mu$m (arrowheads).

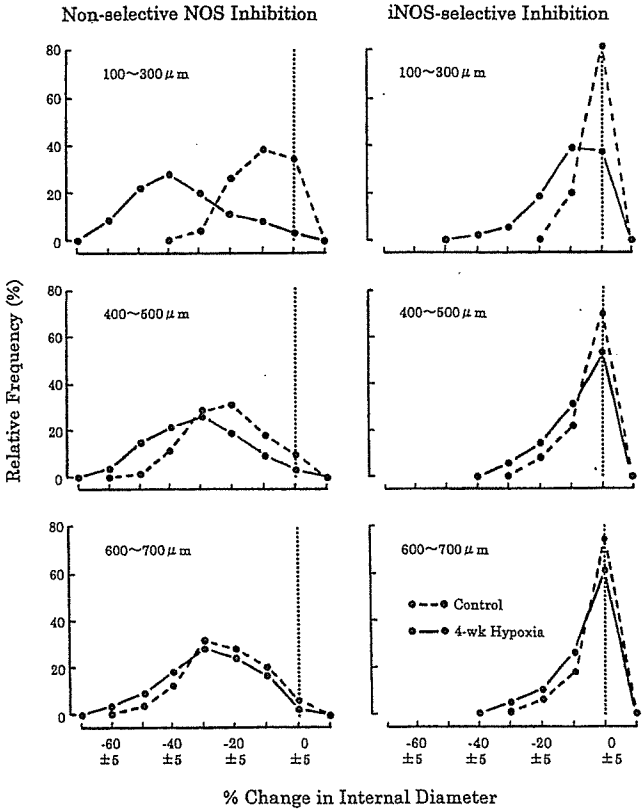

Figure 3 Relative frequency distributions of ID changes due to nonselective NOS inhibition (left) and iNOS-selective inhibition (right) are shown in control (broken line) and chronically hypoxic (solid line) rats. Dotted line indicates no ID change as defined in Methods section. Clear difference in distribution pattern between control and hypoxic rats is seen primarily in muscular pulmonary arteries (100–300 μm) in both types of NOS inhibition.

Effects of PAP increases due to nonselective NOS inhibition on ID

The mechanically induced ~4 mmHg PAP increase had no significant effect on the ID of the muscular and elastic arteries in the CH rat. The mean value of percentage ID change due to the PAP increase for all these arteries was 3±3%.

NOS immunoreactivity changes

Figure 4 shows representative photographs of eNOS immunostaining in the small muscular pulmonary arteries from the control (a) and CH (b) rats. eNOS immunoreactivity was detected in the endothelium of hypoxic arteries (Figure 4b) but not in the control arteries (Figure 4a). Figure 5 shows typical examples of iNOS immunostaining of CH and control rat lungs. The low-magnification view of the hypoxic lung (Figure 5a) showed that an iNOS immunopositive muscular pulmonary artery (arrow) and an iNOS-immunonegative muscular artery (arrowhead) are simultaneously observed in the same section. In the higher-magnification view, the former artery displayed strong iNOS immunostaining primarily in the smooth muscle layers (Figure 5b). However, the latter showed no immunostaining even with higher magnification (Figure 5c). iNOS immunoreactivity was not detected in the control arteries (arrowhead in Figure 5d).

The quantitative data on the distribution of NOS immunoreactivity in the pulmonary arteries of control vs CH lungs are shown in Table 3. In control lungs, eNOS immunoreactivity was distributed only in 9–51% of the muscular arteries, although 91% of the elastic arteries were positive for eNOS. However, the percentage of eNOS-positive vessels greatly increased up to 89–94% in the muscular arteries of CH lungs, while the increase was slight (7%) in the elastic arteries. On the other hand, the percentage of iNOS-positive vessels was small (<10%) in both muscular and elastic arteries of control lungs and increased only to 44–55 and to 68% in these arteries of CH lungs.

Discussion

We quantitatively measured the ID changes of the muscular (resistance) and elastic (conduit) pulmonary arteries in response to different types of NOS inhibitors using an X-ray television system on the control and CH rats under anaesthesia. Moreover, we conducted immunohistochemical analyses to localize NOS proteins in the pulmonary arteries within the control and CH lungs where the ID changes were examined. This was performed to investigate the possible contributions of the hypoxia-induced increase in NOS expres-

Figure 4 eNOS immunostaining of small muscular pulmonary arteries of control (a) and chronically hypoxic (b) rats. eNOS protein was detected in endothelium of hypoxic arteries (arrows), but not in control arteries. Scale bars = 50 μm.